RESEARCH ARTICLE

ADVANCED
ELECTRONIC
MATERIALS
Open Access
www.advelectronicmat.de

C$_8$-BTBT-C$_8$ Thin-Film Transistors Based on Micro-Contact Printed PEDOT:PSS/MWCNT Electrodes

Kirill Gubanov, Manuel Johnson, Melda Akay, Benedikt C. Wolz, Dan Shen, Xing Cheng, Silke Christiansen, and Rainer H. Fink*

Advances in organic materials manufacturing have enabled the creation of electronic devices using solution-processing techniques by employing soluble materials with high conductivity grade. In this exploratory study, the use of micro-contact for poly(3,4-ethylenedioxythiophene) polystyrene sulfonate (PEDOT:PSS) polymer ink deposition as high-quality structured electrodes for organic field-effect transistors (OFETs) in top-contact geometry is demonstrated. The optimized OFET's solution-processed fabrication is a promising strategy to be realized in the simple, cost-effective roll-to-roll manufacturing processes. The electrical performance of the fabricated devices is comparable to transistors with gold electrodes prepared via vacuum deposition, and even exceeding the values of the charge carriers' mobilities and featuring lower contact resistance (R_c), due to lower charge-carrier injection barrier for carbon-based organic electrodes. An addition of multi-walled carbon nanotubes to the PEDOT:PSS decreases R_c even further, changing the work function for better energy alignment with semiconductor materials.

K. Gubanov, M. Johnson, M. Akay, D. Shen, R. H. Fink
Physikalische Chemie II
Friedrich-Alexander-Universität Erlangen-Nürnberg
91058 Erlangen, Germany
E-mail: rainer.fink@fau.de

B. C. Wolz, S. Christiansen
Institute for Nanotechnology and Correlative Microscopy gGmbH
91301 Forchheim, Germany

D. Shen, X. Cheng
Southern University of Science and Technology (SUSTech)
Shenzhen 518055, China

S. Christiansen
Fraunhofer Institute for Ceramic Technologies and Systems IKTS
91301 Forchheim, Germany

S. Christiansen
Physics Department
Freie Universität Berlin
14195 Berlin, Germany

1. Introduction

The field of organic electronics (OE) has made major improvements over the last decades. Many potential applications beyond organic photovoltaics (OPV) such as radio-frequency identification (RFID) systems, organic light-emitting diodes (OLEDs), flexible displays, or organic field-effect transistors (OFETs) are already accessible in the global markets.[1–4] The attraction of organic electronics results from their main advantages over conventional silicon-based technologies such as simple, low-cost and mass production using roll-to-roll technologies, a great potential for modifications and enhancements of the related organic materials electrical properties along with flexibility and transparency.[5] In addition, the substitution of the metal electrodes with conductive polymer materials could offer lower-energy barriers for the charge carriers injection.[6]

The necessity of an effective and scalable patterning technique for low-cost fabrication of organic electronic devices is caused by the fact that some methods, such as ink-jet or screen-printing, have low resolution or involve further process steps, which may affect the performance of the organic materials.[7] Furthermore, techniques like physical vapor deposition (PVD) or chemical vapor deposition (CVD) require high temperatures and vacuum processing, incompatible with the nature of most flexible substrates. In contrast, micro-contact printing (µCP) is an advantageous technique for directly applying materials from an elastomeric stamp that has a patterned relief to a substrate at the area contacted by the stamp, being an etchingless process and capable of patterning high-resolution features.[8,9]

The idea of µCP was introduced in the early 1990s by Whitesides and Kumar for the patterned deposition of thiols onto gold surfaces by means of a microstructured poly(dimethylsiloxane) (PDMS) stamp.[10] From that moment, a broad variety of different modifications and improvements of the method have been made,[11,12] such as magnetic field assistance for homogeneous pressure during the printing step, by injecting an iron powder into a layer of the PDMS,[13] or so-called submerged printing, involving a liquid medium for stamp support.[14] The µCP technique has been mostly used for the patterning of
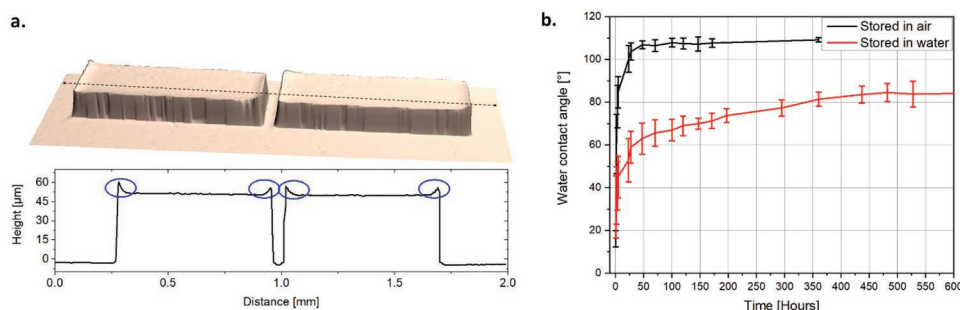
Figure 1. a) 3D map of PDMS stamp with corresponding height profile. b) Change of water contact angle over the time for PDMS stamp kept at air (black curve) and in water (red curve).

self-assembled monolayers (SAMs) or catalysts for electroless deposition.[15] Recently, Takakuwa et. al. successfully applied the µCP method for electrodes patterning using PEDOT:PSS.[9] However, the reported electrical performance of the fabricated OFETs required further improvements due to high contact resistances (R_C) and high threshold voltages.

Within this exploratory study, we employed an optimized µCP method for PEDOT:PSS electrodes preparation by controlling the contact pressure and surface free energy of the PDMS elastomer stamp by oxygen plasma pretreatment.[15] As a highly conductive polymer PEDOT:PSS is a promising electrode material for applications in OFETs, since it is a water-soluble polyelectrolyte system with good film-forming properties.[16] PEDOT:PSS films have high thermal stability as they can withstand heating up to 100 °C for over 1000 h with only slight changes in conductivity.[17] Despite all undeniable advantages of PEDOT:PSS material the issue of quite high R_C remains to be solved.[18] In this regard, we have chosen a simple strategy by adding multi-walled carbon nanotubes (MWCNTs) into PEDOT:PSS. MWCNTs serve as a conductive filler in polymer composite films polymers by the formation of conductive channels within the PEDOT:PSS matrix.[19] In addition, the π-π interactions between the MWCNTs and the PEDOT backbone leads to an electron density transfer to the PEDOT:PSS.[20] Previous studies have also shown that MWCNTs are significantly more resistant against the mechanical stress rather than their counterparts (i.e., single-walled CNTs), which is a big advantage within the µCP process.[21] Moreover, MWCNTs are remarkably better for operation in strongly corrosive ambience demonstrating lower oxygen reduction as compared with SWCNTs.[22] As organic p-type semiconductor in our OFETs, we use solution-processed 2,7-dioctyl[1]benzothieno[3,2-b]benzothiophene (C_8-BTBT-C_8) films. Dialkylated BTBT has attracted significant attention due to its quite high hole mobility (up to 43 cm^2 V^{-1} s^{-1} for optimized devices).[23–25] The good solubility of C_8-BTBT-C_8 results from the integrated alkyl chain into its core structure.[26] We demonstrate a simple and advantageous fabrication process of top-contact/bottom-gate OFETs[27–29] using a µCP method which offers a low cost and efficient production of PEDOT:PSS electrodes on the micrometer-scale level. Moreover, we have investigated the effect of the MWCNTs introduced into the electrode material resulting in an increased electrical conductivity and reduced contact resistance in contrast with conventional PEDOT:PSS material.

2. Experimental Section

2.1. PDMS Stamp Fabrication

The master mold with the stamp structure cells of different sizes was produced by conventional nanolithography. The channel lengths in between the contacts vary from 500 µm down to 10 µm. Sylgard 184 (Dow Corning Co., USA) elastomer base and curing agent were mixed in a 10:1 ratio inside a plastic vessel and continuously stirred for several minutes. Such mixing ratio was chosen in order to create stamps with the middle stiffness.[15] Afterward, the vessel was placed in vacuum chamber and kept at 0.1 mbar in order to degas the mixture and draw an air to the surface. Then, the PDMS mixture was carefully poured onto a mold filling the stamp structure cells and kept again at 0.1 mbar for 1 h. The assembly was then placed inside an oven and heated up to 100 °C. After one hour, the PDMS stamp was removed from the mold. The fabrication flow of the stamps displayed in Figure S1 (Supporting Information) had made major improvements over the last decades. **Figure 1**a provides a 3D optical map of the fabricated PDMS stamp with very well defined structural quality. The height profiles clearly indicate the protruding edges at the stamp structure (blue circles), which may appear during the detachment of the stamp from the mold. Such barriers were beneficial for keeping PEDOT:PSS films within the desired shape during subsequent spin-coating.

In order to spin-cast a high-conductivity grade aqueous solution of PEDOT:PSS onto the stamp, it was necessary to change the PDMS hydrophobic nature to hydrophilic.[30] Oxygen plasma treatment (200 W, 0.2 mbar, 30 s) had been applied, introducing polar functional silanol groups (SiOH) and changing PDMS surface properties.[31] Figure 1b shows the temporal development of the water contact angle (CA) after plasma processing. Right after oxygen plasma treatment, the stamp surface was highly hydrophilic as indicated by the water CA of ≈10°. Within the next ≈4 h of storing the stamp in the air, the CA rapidly increased up to ≈70°. The measurements after ≈70 h demonstrated that the PDMS stamp is hydrophobic again with a water CA > 90°. In order to achieve a long-term preservation of the oxygen plasma-hydrophilization, PDMS could be stored in water.[32,33] Within the first few hours, we indicated almost the same hydrophobic recovery (red curve), however the CA was kept constant at ≈50° for several days, prolonging the stamp performance. In recent study, Tserepi and Gogolides

**ADVANCED
SCIENCE NEWS**

www.advancedsciencenews.com

**ADVANCED
ELECTRONIC
MATERIALS**

www.advelectronicmat.de

examined the morphological changes of PDMS surface after oxygen-plasma treatment.[34] Atomic force microscopy (AFM) showed that the surface treatment significantly increases the surface roughness as a function of O_2 plasma exposure time. This can be explained by high mechanical stress of the material that originates from the high PDMS viscoelasticity.[35]

2.2. OFET Device Fabrication

Figure 2 shows the fabrication workflow of our C_8-BTBT-C_8-based OFETs with structured PEDOT:PSS electrodes in top-contact geometry. A p-doped Si wafer was used as a substrate with additional 46 nm film of aluminum oxide dielectric to allow low operation voltages and to decrease the hysteresis in OFET characteristics.[36,37] First, a film of C_8-BTBT-C_8 was spin-cast from toluene (2.5 mg mL) with 2500 rpm for 40 s onto the Al_2O_3 insulating film. Afterward, PEDOT:PSS ink (3–4 wt% aqueous solution) with added MWCNTs (0.15 wt%) was spin-cast (2500 rpm for 40 s) on the elastomer stamp after PDMS surface treatment as described above. Next, the stamp with PEDOT:PSS/MWCNTs film composite was pressed onto the C_8-BTBT-C_8 film for 30 s controlling the pressure with a high-precision laboratory balance. Finally, the PDMS stamp was removed resulting in well-defined PEDOT:PSS patterns on the coated C_8-BTBT-C8 surface (see results). All chemicals, i.e., toluene (ACS reagent grade), C_8-BTBT-C_8 (≥99% (HPLC) grade), PEDOT:PSS (3-4% high-conductivity grade) and MWCNTs (≥90% carbon basis, average diameter and length: 150 nm and 7 μm, respectively) were purchased from Sigma-Aldrich and used as delivered.

2.3. Characterization Tools

Water contact angle measurements were performed in static mode using a Dataphysics optical contact angle and contour analysis 25 (OCA 25). 3D confocal images were taken with an optical surface metrology system Leica DCM 3D with objectives ranging from 5× (NA 0.15) to 150× (NA 0.95). Optical microscopy images were recorded with a Leica DM 4000 M microscope equipped with a Leica DFC 320 camera. AFM measurements were performed with a JPK Nanowizard 4 in non-contact mode. For scanning electron microscopy (SEM) a ZEISS EVO 50 operating at 10 kV was used. For 3D elemental analysis, focused ion beam (FIB) sectioning was combined with energy-dispersive X-ray analysis (EDX) elemental mapping using a Zeiss XB550 equipped with an Oxford Ultra Max (150 mm²). Viscosity of the PEDOT:PSS inks was measured using a Schott 513-01 capillary viscometer. Resistivity measurements were performed using a Keithley 2450 SourceMeter SMU with a four-point collinear probe. Raman spectroscopy and mapping analysis were performed using a Horiba Labram HR Evolution spectrometer with 532 nm irradiation (2.1 W laser power, 50× objective, NA 0.75).

3. Results and Discussion

3.1. Microscopic Characterization

Figure 3 summarizes the findings from the morphology analysis of the fabricated OFETs. We have used the contacts with 50 μm gap (in the PDMS master). Visible light microscopy (Figure 3a) shows that the patterns were successfully transferred onto the semiconductor layer with a fine structural quality and defined channel length. The color changes within the printed PEDOT:PSS contacts results from thickness dependent interferences indicating thickness variations at the rims but also within the contacts (see discussion below).

Figure 3b shows a SEM image of the PEDOT:PSS/MWCNT composite film. The carbon nanotubes are uniformly distributed and debundled within the PEDOT:PSS polymer matrix. The presence of the MWCNTs was confirmed by Raman mapping (see Figure S2, Supplementary Information). Figure 3c shows a 3D topographic map of the well-defined channel region in between two μ-contact printed PEDOT:PSS/MWCNT composite electrodes. The corresponding cross-sectional profile is shown in Figure 3d indicating a channel width of about 55 μm. The 3D map reveals the thinner flat regions next to the active channel and the elevated parts of both electrodes. The AFM image (Figure 3e) shows the morphology for the channel area with the spin-cast C_8-BTBT-C_8, which is known to form the typical layer and island structure.[43,44] The channel width of the inspected region is about 60 μm and thus in close agreement with the optical 3D microscopy. The height of the
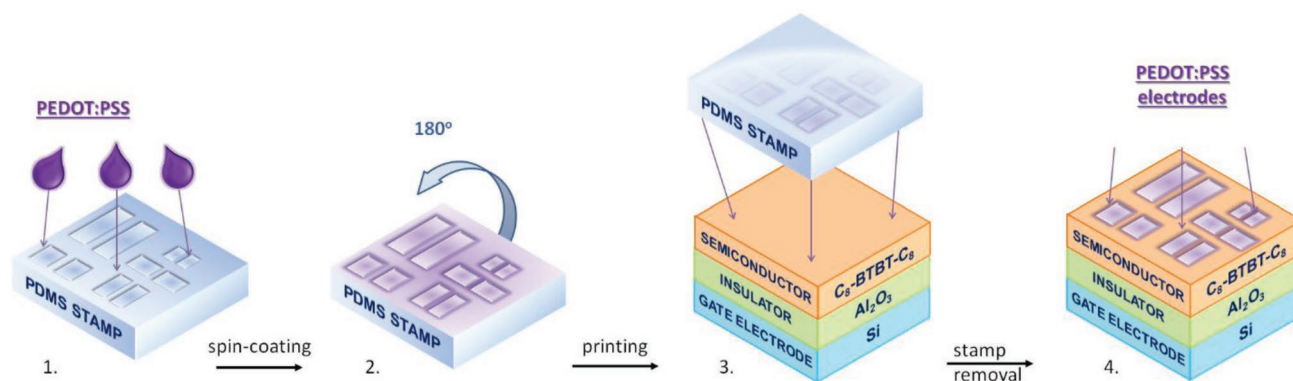

Figure 2. Workflow of the contact fabrication process of C_8-BTBT-C_8-based OFETs using the μCP technique.

**ADVANCED
SCIENCE NEWS**
www.advancedsciencenews.com

**ADVANCED
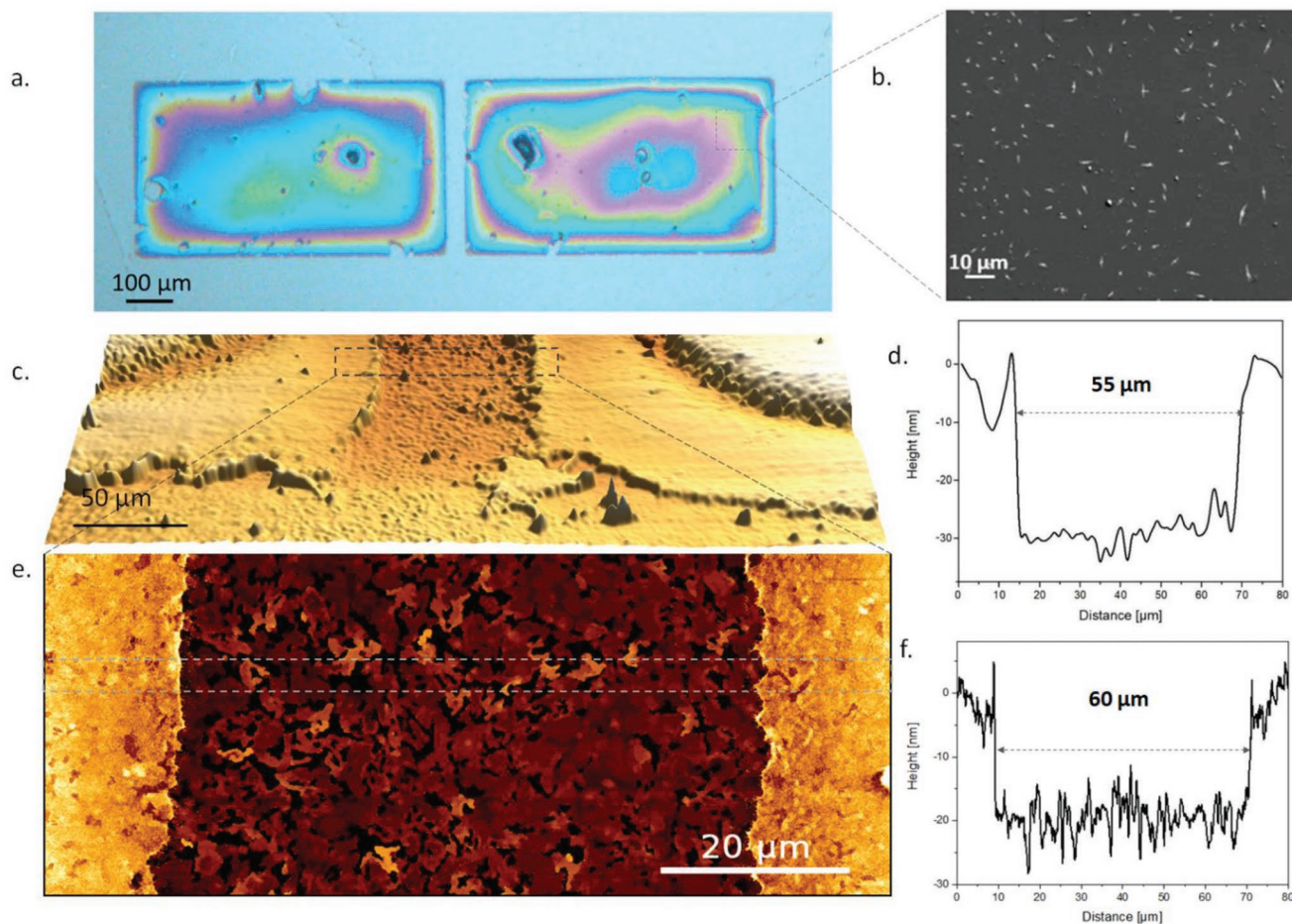ELECTRONIC
MATERIALS**
www.advelectronicmat.de

Figure 3. a) Optical microscopy image of an exemplary µCP-printed OFET device with spin-cast C_8-BTBT-C_8 and PEDOT.PSS/MWCNT composite electrode. The gap in the PDMS stamp is 50 µm. b) SEM image of the contact region indicating an almost homogeneous distribution of MWCNTs. c) 3D optical microscopy image of the contact/channel region with d) corresponding height profile (averaged over 30 scan lines) e) AFM image and f) corresponding cross-section (averaged over 30 scan lines).

PEDOT:PSS/MWCNT electrodes derived from the AFM profiles is about 20 nm giving a hint that 3D optical microscopy overestimates the true height (see Figure 3f).

The question arises why the produced contact widths deviate from the original structures of the PDMS master, i.e., 50 µm gaps. The answer may be two-fold. First, we must consider the viscosity of the polymer composite as it is documented in the literature, that viscosity of the polymer affects the film uniformity.[38–42] We found that the PEDOT:PSS/MWCNTs ink solution is slightly more viscous (7.98×10^{-4} m^2 s^{-1}) compared to the pure PEDOT:PSS ink (8.81×10^{-5} m^2 s^{-1}). Therefore, already the spin-casting of the composite may lead to nonuniform films on the PDMS stamp prior to printing. Second, the highly viscous polymer retracts during the release of the stamp after polymer transfer onto the semiconducting film and subsequent evaporation of the water from the polymer leaving behind a relatively thin PEDOT:PSS regime next to the semiconducting channel (see Figure 3c).

The effect of rim modification of the printed contacts becomes particularly obvious when we apply higher pressures during pattern transfer. **Figure 4** shows AFM images of the edge area between a printed composite electrode (right-hand

side) and an underlying C_8-BTBT-C_8 film (left-hand side) for the different pressures applied on the stamp during the printing. For highest applied pressures (Figure 4a) we found that the stamp simply removes the parts of the electrode upon retraction, leaving a gap between the electrode and semiconductor material. We found that even for the lower mechanical loads the pressure needs to be adjusted carefully. Figure 4b reveals an inter-region between the electrode and semiconductor film, yet with a significantly lower coverage of the PEDOT:PSS material. Finally, the optimized pressure for transferring the electrode patterns with no gaps or subsequent material removal was found to be 2.0 MPa (Figure 4c).

Besides the influence of the inks viscosity, we attribute this finding to the nature of the PDMS elastomer material, a loosely cross-linked polymer subclass with flexibility and elasticity features of the rubber and low Young's modulus of 3 MPa.[45,46] This material can easily expand and then return to its original size when the applied force is removed.[47] We observe this effect, when applying a pressure on PDMS structure higher than its Young's modulus (see Figure S3, Supporting Information). For printing with pressures higher than 3 MPa, the stamp expands and after lifting it up, shrinks back, removing
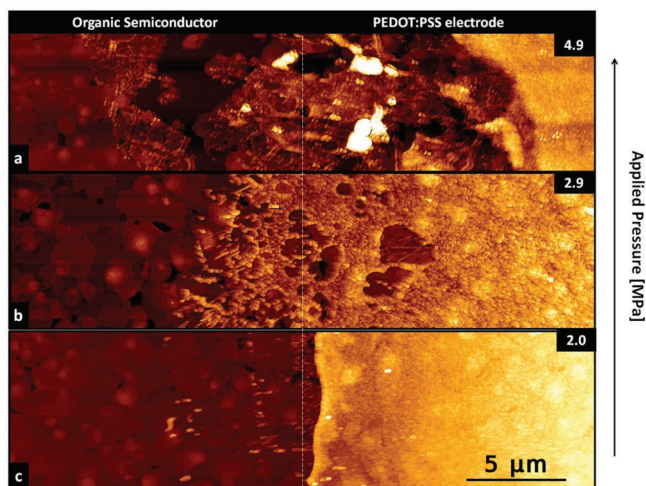
Figure 4. a-c) AFM images (non-contact mode) displaying the area between a μ-contact printed PEDOT:PSS/MWCNT composite electrode (right-hand side) and an underlying C_8-BTBT-C_8 film (left-hand side) for different applied pressures (in MPa indicated in the top right).

the part of the printed pattern, while with the 2 MPa, the material removal does not occur.

Having studied the surface morphology of the electrodes and semiconductor, we now address the internal arrangements of the resulting OFET device, in particular on the quality of the internal interfaces. **Figure 5** shows the EDX elemental mapping of the FIB-SEM cross-sectional area of the fabricated OFET with printed electrodes, revealing the distribution of different elements for each layer of produced device. A layer of gold

(80 nm) was sputtered on top of the sample in order to ensure better surface protection during the FIB milling. In order to better preserve the organic materials from ion beam damage, low ion acceleration voltage (2 kV) was used for FIB-SEM cross-sectioning. This explains the wedge shape of the FIB area (Figure 5a). Under these conditions the ion spot is bigger and less defined than for standard 30 kV. For higher acceleration voltages, the C_8-BTBT-C_8 semiconductor film was removed completely.

Compositional maps confirm the presence of all elements expected and hence prove the clear separation between each layer of the produced OFET. In particular, Figure 5d shows very low intensity of the oxygen signal for the oxygen-free semiconductor region, yet carbon (Figure 5e) and sulfur (Figure 5f) are present, excluding the vanishing or intermixing of C_8-BTBT-C_8 with the printed electrode material. In addition, aluminum (Figure 5c) and oxygen signals reveal a clearly defined Al_2O_3 dielectric film.

3.2. Electrical Evaluation

For electrical characterization C_8-BTBT-C_8 based devices with varying channel length of 40, 50, 100, 150 and 200 μm and printed PEDOT:PSS/MWCNTs electrodes were measured. The charge carrier mobility was calculated from the slope of the square root of drain current versus the gate voltage by fitting the data to Equation (1):

$$I_d = \left(\frac{WC_i}{2L}\right)\mu_{FET}\left(V_G - V_{th}\right)^2 \tag{1}$$
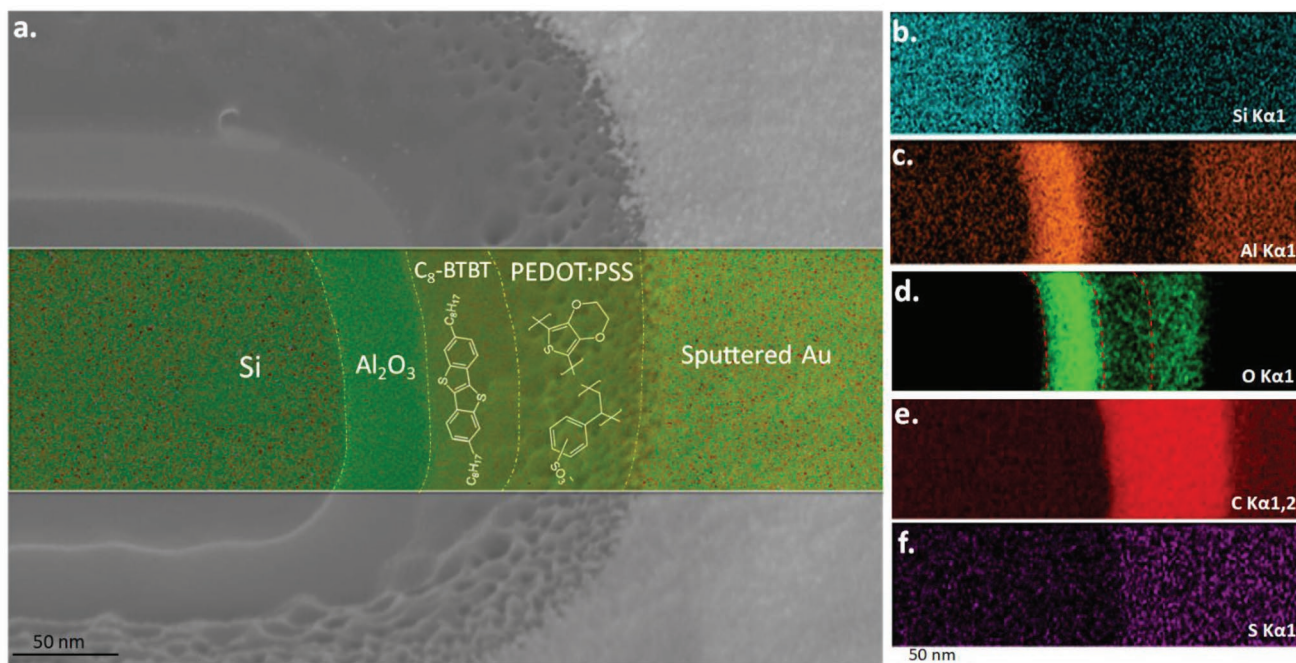

Figure 5. a) FIB-SEM image and EDX cross-sectional mapping of the fabricated OFET. b–f) The EDX elemental color mapping of silicon (b), aluminum (c), oxygen (d), carbon (e), and sulfur (f) as a selective portion of cross-section (a). To reduce the negative impact from electrons and ions, low-energetic electrons (2 keV at 500 pA) and Ga^+ ions (5 keV at 200 pA) were used for EDX imaging and structure preparation, respectively.
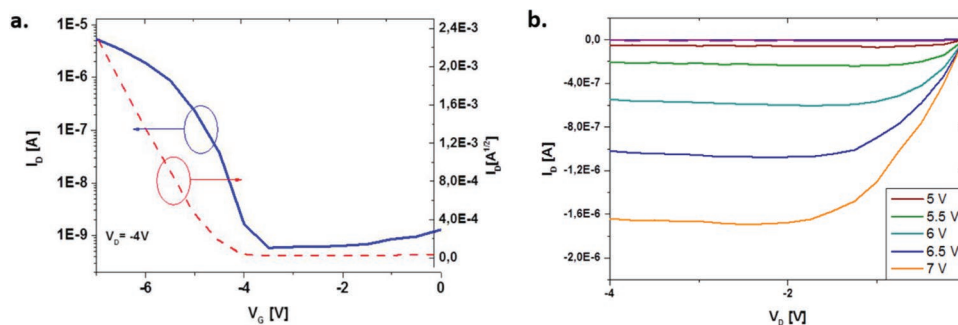
Figure 6. a,b) Transfer (a) and output (b) curves for OFETs with spin-cast C_8-BTBT-C_8 and micro-contact-printed PEDOT:PSS/MWCTNs composite electrodes (channel length: 40 µm).

where I_D is the drain current, W and L are gate width and length respectively, μ is the charge carrier mobility, V_G is the gate voltage, V_{th} is the threshold voltage and C_i as the Al_2O_3 insulator capacitance.

Figure 6 shows transfer and output characteristics for C_8-BTBT-C_8 based OFETs with µ-contact printed PEDOT:PSS/ MWCNTs source and drain contacts. All devices show p-type characteristics with a linear current increase at small drain voltages and a saturation regime at larger drain voltages ($V_D > 2$ V). From the transfer curves an average mobility μ_{FET} in the saturation regime (–4 V_D/–7 V_G) of 0.6 ± 0.3 cm^2 V^{-1} s^{-1} with a threshold voltage V_{th} of –4.3 ± 0.6 V and an on/off current ratio around 3×10^3 were extracted. Additionally, we prepared reference samples with vacuum-sublimated gold electrodes as source and drain contacts (Au thickness 40 nm, deposited through a shadow mask). For thus prepared devices, we obtained an average mobility μ_{FET} of ≈0.3 ± 0.2 cm^2 V^{-1} s^{-1}, a similar on/off current ratio of 3×10^3 and a threshold voltage V_{th} of –1.8 V.

Comparing both types of the devices, we found that OFETs with PEDOT:PSS/MWCNTs electrodes yield a higher charge carrier mobility as OFETs prepared with conventional vacuum-sublimated gold electrodes (**Table 1**).

Since in both cases we used a top-contact device geometry and identical preparation condition for the organic layer, the morphology of the C_8-BTBT-C_8 thin film is expected similar for both types of devices. We therefore attribute the increased device performance to a lower charge carrier injection barrier at the PEDOT:PSS/C_8-BTBT-C_8 interface as compared to the Au/ C_8-BTBT-C_8 interface. Similar behavior was found for pentacene based OFETs with printed PEDOT:PSS as well as PEDOT:PSS-coated Au electrodes.[48,49]

To further investigate the differences between PEDOT:PSS/ MWCNT and gold electrodes, the contact resistance (R_C) was determined. The most common way to extract the R_C for

field-effect transistors in general, is the so-called transfer-line method (TLM).[50,51] This method utilizes the fact, that in the linear regime, the device can be described as series of resistances, assuming a channel resistance (that depends on the channel length) and the contact resistance (independent from the channel length). This leads to Equation (2) and by plotting the measured total resistance (R_{tot}) against the channel length L a straight line can be fitted, where the y-intercept equals R_C.

$$R_{tot}W = \frac{L}{\mu C_i (V_G - V_{th})} + R_{sd}W \tag{2}$$

While TLM possesses a simple way to estimate the contact resistance, it requires a set of devices with several channel lengths and its accuracy is severely limited by a large parameter distribution, especially μ and V_{th}, usually existing in solution prepared OFETs. A more reliable method to extract the contact resistance for sets with only few different channel lengths and larger device-to-device variations, is the modified transfer-line method (M-TLM) introduced by Xu et al.[50] In this approach, Equation (2) is divided by L so that slope is controlled by contact resistance (Equation (3)).

$$\frac{R_{tot}W}{L} = \frac{1}{\mu C_i (V_G - V_{th})} + (R_{sd}W)\frac{1}{L} \tag{3}$$

Thus, R_C can be estimated more accurately since the slope of the linear fit is less sensitive to parameter variations than the intercept.[53] **Figure 7**a shows the M-TLM plot for devices with hybrid PEDOT:PSS/MWCNTs electrodes at several gate voltages from which R_C was determined according to Equation (3).

The values of the width-normalized contact resistance, plotted as a function of the applied gate voltage are displayed in Figure 7b. Here, the values for the reference samples with conventional Au source and drain contacts are shown for comparison. For both devices we observe that the contact resistance decreases with an increasing gate bias. This gate–voltage dependence is caused by the staggered device structure, which leads to an accumulation of charge density and therefore a reduced sheet resistance below the source contact.[54,55] The extracted R_C for the vacuum-deposited Au electrodes is around 260 kΩ cm at –5.5 V and decreased to 180 kΩ cm at a gate voltage of –7 V while the extracted contact resistance of printed PEDOT:PSS/MWCNTs electrodes was around 31 % lower, i.e., 180 kΩ cm at –5.5 V and around 124 kΩ cm at –7 V.

Table 1. Averaged extracted threshold voltages, on/off ratio and charge-carrier mobilities for µCP and vacuum sublimated reference samples.

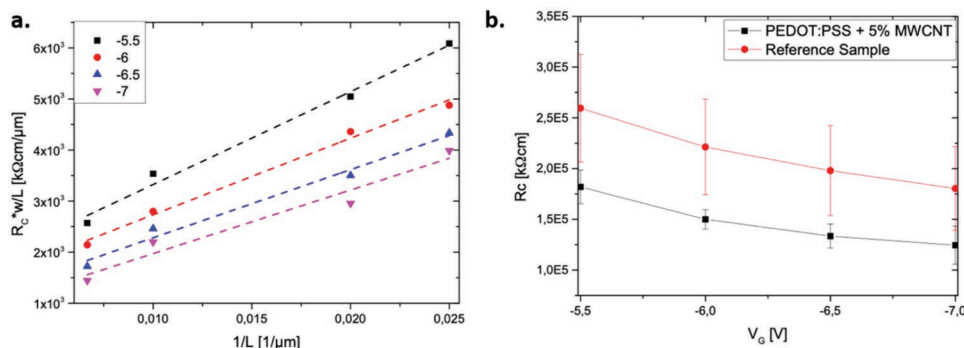| Device	PEDOT:PSS with 0.15 wt% MWCNTs	Reference sample with Au electrodes
V_{th}	–4.3 ± 0.6 V	–1.8 ± 0.4 V
$I_{on/off}$	3.3×10^3	3.0×10^3
μ_{FET}	0.6 ± 0.3 cm^2 V^{-1} s^{-1}	0.29 ± 0.2 cm^2 V^{-1} s^{-1}

Figure 7. a) M-TLM plot for OFETs with spin-cast C_8-BTBT-C_8 and micro-contact-printed electrodes. b) Width normalized contact resistance as function of gate voltage for OFETs with PEDOT:PSS/MWCNTs (black symbols) and vacuum-deposited Au electrodes (red symbols).

Despite the 0.1 eV lower work function for the PEDOT:PSS/MWCNTs composite film, devices fabricated with organic electrodes showed an increased performance, e.g., higher mobility and lower contact resistance, compared to reference devices with vacuum sublimated Au electrodes. Since we use a top-contact geometry and the preparation of the organic layer is similar for both type of devices, morphological differences are not expected to change the device performance. We therefore attribute this to the more efficient hole injection due to a lower injection barrier from the PEDOT:PSS/MWCNTs electrode to the organic layer.

4. Conclusions

We successfully prepared C_8-BTBT-C_8 based OFETs with high-quality microcontact-printed PEDOT:PSS electrodes of various channel lengths in the micrometer regime. The precise control of the contact pressure during the printing process is important to reduce the stamp deformation and avoid the morphological damage to the active C_8-BTBT-C_8 semiconductor film. The cross-section elemental analysis demonstrated the proper internal arrangement between the organic films, excluding the material intermixture or damage. By virtue of the device fabrication simplicity, low-cost, high structural quality, as well as competitive electrical performance, it is a promising strategy to be applied in the large-scale manufacturing processes, such as roll-to-roll electronics production.

To increase the PEDOT:PSS conductivity, the polymer was mixed with MWCNTs. Spin-cast thin films with different MWCNTs concentrations displayed a decrease in sheet resistance (Figure S4, Supporting Information) and work function with increasing nanotubes ratio. Moreover, the addition of MWCNTs to the PEDOT:PSS electrodes leads to a reduction of contact resistance caused by the formation of conductive channels inside the PEDOT:PSS matrix and reduced charge carrier injection barrier in comparison with unmodified PEDOT:PSS/C_8-BTBT-C_8 or even Au/C_8-BTBT-C_8 interface. For further electrical performance improvements, the device geometry can be changed to the bottom-contact type, preventing the morphological discontinuity of the organic semiconductor and source/drain electrodes.

Supporting Information

Supporting Information is available from the Wiley Online Library or from the author.

Conflict of Interest

The authors declare no conflict of interest.

Data Availability Statement

The data that support the findings of this study are available from the corresponding author upon reasonable request.

[1] S. Logothetidis, *Handbook of Flexible Organic Electronics: Materials, Manufacturing and Applications*, Woodhead Publishing, Cambridge, UK **2015**.

[2] V. Subramanian, J. M. J. Frechet, P. C. Chang, D. C. Huang, J. B. Lee, S. E. Molesa, A. R. Murphy, D. R. Redinger, S. K. Volkman, *Proc. IEEE* **2005**, *93*, 1330.

[3] J.-J. Kim, M.-K. Han, Y.-Y. Noh, *Semicond. Sci. Technol.* **2011**, *26*, 030301.

[4] C. Wöll, *Organic Electronics: Structural and Electronic Properties of OFETs*, Wiley-VCH Verlag, Weinheim, Germany **2009**.

[5] C. S. Buga, J. C. Viana, *Adv. Mater. Technol.* **2021**, *6*, 2001016.

[6] X. Cheng, Y.-Y. Noh, J. Wang, M. Tello, J. Frisch, R.-P. Blum, A. Vollmer, J. P. Rabe, N. Koch, H. Sirringhaus, *Adv. Funct. Mater.* **2009**, *19*, 2407.

[7] J. Lewis, *Mater. Today* **2006**, *9*, 38.

[8] T. Kaufmann, B. J. Ravoo, *Polym. Chem.* **2010**, *1*, 371.

[9] A. Takakuwa, M. Ikawa, M. Fujita, K. Yase, *Jpn. J. Appl. Phys.* **2007**, *46*, 5960.

[10] A. Kumar, H. A. Biebuyck, N. L. Abbott, G. M. Whitesides, *J. Am. Chem. Soc.* **1992**, *114*, 9188.

[11] S. G. Ricoult, M. Pla-Roca, R. Safavieh, G. M. Lopez-Ayon, P. Grütter, T. E. Kennedy, D. Juncker, *Small* **2013**, *9*, 3308.

[12] H. Lalo, J. C. Cau, C. Thibault, N. Marsaud, *Microelectron. Eng.* **2009**, *86*, 1428.

[13] J.-C. Cau, L. Lafforgue, M. Nogues, A. Lagraulet, V. Paveau, *Microelectron. Eng.* **2013**, *110*, 207.

[14] F. Bessueille, M. Pla-Roca, C. A. Mills, E. Martinez, J. Samitier, A. Errachid, *Langmuir* **2005**, *21*, 12060.

[15] H. Lee, D. Koh, L. Xu, S. Row, S. T. Andreadis, K. W. Oh, *Micromachines* **2016**, *7*, 173.

[16] M. Dobbelin, R. Marcilla, C. Pozo-Gonzalo, D. Mecerreyes, *J. Mater. Chem.* **2010**, *20*, 7613.

[17] J. Huang, P. F. Miller, J. C. de Mello, A. J. de Mello, D. D. C. Bradley, *Synth. Met.* **2003**, *139*, 569.

[18] S. Pretl, A. Hamacek, J. Reboun, J. Stulik, in *2012 4th Electronic System-Integration Technology Conf.*, IEEE, Piscataway, NJ, USA **2012**, https://doi.org/10.1109/ESTC.2012.6542214.

[19] J. Li, J. Liu, C. Gao, *Int. J. Photoenergy* **2009**, *5*, 650509.

[20] J. Li, J. Liu, C. Gao, *J. Polym. Sci. (N. Y., NY, U. S.)* **2010**, *17*, 713.

[21] E. M. Byrne, M. A. McCarthy, Z. Xia, W. A. Curtin, *Phys. Rev. Lett.* **2009**, *103*, 045502.

[22] M. S. Mousa, *IOP Conf. Ser.: Mater. Sci. Eng.* **2018**, *305*, 012025.

[23] H. Shin, K. Baek, H. Yun, Y. Ham, K. Park, G. Lee, H. Lee, J. Wang, K. Lee, L. Do, *IMID* **2009**, *55*, 1118.

[24] H. Ren, Q. Tang, Y. Tong, Y. Liu, *Materials* **2017**, *10*, 918.

[25] Y. Yuan, G. Giri, A. L. Ayzner, A. P. Zoombelt, S. C. B. Mannsfeld, J. Chen, D. Nordlund, M. F. Toney, J. Huang, Z. Bao, *Nat. Commun.* **2014**, *4005*, 3005.

[26] C. Wang, H. Dong, W. Hu, Y. Liu, D. Zhu, *Chem. Rev.* **2012**, *112*, 2208.

[27] C. H. Kim, Y. Bonnassieux, G. Horowitz, *IEEE Electron Device Lett.* **2011**, *32*, 1302.

[28] T. Marszalek, A. Nosal, R. Pfattner, J. Jung, S. Kotarba, M. Mas-Torrent, B. Krause, J. Veciana, M. Gazicki-Lipman, C. Crickert, G. Schmidt, C. Rovira, J. Ulanski, *Org. Electron.* **2012**, *13*, 121.

[29] M. Chen, L. Yan, Y. Zhao, I. Murtaza, H. Meng, W. Huang, *J. Mater. Chem.* **2018**, *6*, 7416.

[30] M. Kakuta, F. Bessoth, A. Manz, *Chem. Rec.* **2001**, *1*, 395.

[31] H. Hillborg, J. F. Ankner, U. W. Gedde, G. D. Smith, H. K. Yasuda, K. Wikström, *Polymer* **2000**, *6851*, 41.

[32] A. Gökaltun, Y. B. (A.) Kang, M. L. Yarmush, O. B. Usta, A. Asatekin, *Sci. Rep.* **2019**, *9*, 7377.

[33] F. Jahangiri, T. Hakala, V. Jokinen, *Microfluid. Nanofluid.* **2020**, *24*, 2.

[34] A. Tserepi, E. Gogolides, K. Tsougeni, V. Constantoudis, *J. Appl. Phys.* **2005**, *98*, 113502.

[35] R. Raveendran, M. A. G. Namboothirty, *ASC Omega* **2018**, *3*, 11278.

[36] M. Egginger, S. Bauer, R. Schwödiauer, H. Neugebauer, N. S. Sariciftci, *Monatsh. Chem.* **2009**, *140*, 735.

[37] G. Houin, F. Duez, L. Garcia, E. Cantatore, L. Hirsch, D. Belot, C. Pellet, M. Abbas, *Flex. Print. Electron.* **2017**, *2*, 045004.

[38] F. Zabihi, Y. Xie, S. Gao, M. Eslamian, *Appl. Surf. Sci.* **2015**, *338*, 163.

[39] A. Singh, M. Katiyar, A. Garg, *RSC Adv.* **2015**, *5*, 78677.

[40] J. Griffin, A. J. Ryan, D. G. Lidzey, *Org. Electron.* **2017**, *41*, 245.

[41] L. Hu, J. Song, X. Yin, Z. Su, Z. Li, *Polymers* **2020**, *12*, 145.

[42] J. Liou, P. H. Hsu, W. R. Chen, D. W. Chou, K. W. Lee, N. F. Wang, S. W. Feng, C. J. Huang, *Sens. Mater.* **2019**, *31*, 211.

[43] J. H. Lee, S. Kim, H. Kim, J. Lee, *Org. Electron.* **2018**, *52*, 184.

[44] L. Lyu, D. Nie, H. Xie, Y. Zhao, N. Cao, H. Zhang, Y. Zhang, P. Liu, Y. Gao, *Phys Chem Chem Phys* **2017**, *19*, 1669.

[45] V. R. Sastri, *Plastics and Medical Devices: Properties, Requirements and Applications*, William Andrew/Elsevier, Burlington, MA, USA **2010**.

[46] L. Fillipponi, P. Livingston, O. Kaspar, V. Tokarova, D. V. Nicolau, *Biomed. Microdevices* **2016**, *18*, 9.

[47] S. K. De, J. R. White, *Rubber Technologist's Handbook*, Rapra Technologies Ltd, Shrewsbury, UK **2001**.

[48] D. Li, L. J. Guo, *Appl. Phys. Lett.* **2006**, *88*, 063513.

[49] K. Hong, S. Y. Yang, C. Yang, S. H. Kim, D. Choi, C. E. Park, *Organ. Electron.* **2008**, *9*, 864.

[50] G. Horowitz, *J. Mater. Res.* **2004**, *19*, 1946.

[51] D. J. Gundlach, L. Zhou, J. A. Nichols, T. N. Jackson, *J. Appl. Phys.* **2006**, *100*, 024509.

[52] Y. Xu, R. Gwoziecki, I. Chartier, R. Coppard, F. Balestra, G. Ghibaudo, *Appl. Phys. Lett.* **2010**, *97*, 171.

[53] M. Waldrip, O. D. Jurchescu, D. J. Gundlach, E. G. Bittle, *Adv. Funct. Mater.* **2020**, *30*, 1904576.

[54] G. de Tournadre, F. Reisdorffer, R. Rödel, O. Simonetti, H. Klauk, L. Giraudet, *J. Appl. Phys.* **2016**, *119*, 125501.

[55] R. Rödel, F. Letzkus, T. Zaki, J. N. Burghartz, U. Kraft, U. Zschieschang, K. Kern, H. Klauk, *Appl Phys Lett* **2013**, *102*, 233303.